CrossMark

The Asian–Bering–North American teleconnection: seasonality, maintenance, and climate impact on North America

Bin Yu[1] · H. Lin[2] · Z. W. Wu[3] · W. J. Merryfield[4]

Abstract The Asian–Bering–North American (ABNA) teleconnection index is constructed from the normalized 500-hPa geopotential field by excluding the Pacific–North American pattern contribution. The ABNA pattern features a zonally elongated wavetrain originating from North Asia and flowing downstream across Bering Sea and Strait towards North America. The large-scale teleconnection is a year-round phenomenon that displays strong seasonality with the peak variability in winter. North American surface temperature and temperature extremes, including warm days and nights as well as cold days and nights, are significantly controlled by this teleconnection. The ABNA pattern has an equivalent barotropic structure in the troposphere and is supported by synoptic-scale eddy forcing in the upper troposphere. Its associated sea surface temperature anomalies exhibit a horseshoe-shaped structure in the North Pacific, most prominent in winter, which is driven by atmospheric circulation anomalies. The snow cover anomalies over the West Siberian plain and Central Siberian Plateau in autumn and spring and over southern Siberia in winter may act as a forcing influence on the ABNA pattern. The snow forcing influence in winter and spring can be traced back to the preceding season, which provides a predictability source for this teleconnection and for North American temperature variability. The ABNA associated energy budget is dominated by surface longwave radiation anomalies year-round, with the temperature anomalies supported by anomalous downward longwave radiation and damped by upward longwave radiation at the surface.

✉ Bin Yu
  Bin.Yu@canada.ca

1   Climate Research Division, Environment and Climate
    Change Canada, 4905 Dufferin Street, Toronto,
    ON M3H 5T4, Canada

2   Meteorological Research Division, Environment and Climate
    Change Canada, Dorval, Canada

3   Institute of Atmospheric Sciences, Fudan University,
    Shanghai, China

4   Canadian Centre for Climate Modelling and Analysis,
    Environment and Climate Change Canada, Victoria, Canada

1 Introduction

The impact of the tropical sea surface temperature (SST) anomaly, in particular the El Niño–Southern Oscillation (ENSO) variability, on North American climate has been extensively investigated (e.g., Ropelewski and Halpert 1986; Trenberth et al. 1998; Liu and Alexander 2007; and references therein). For example, the Pacific–North American (PNA, Wallace and Gutzler 1981) pattern, one of the most prominent teleconnections in the Northern Hemisphere winter that impacts North American climate, is found to be influenced by ENSO events. Hence understanding the tropical SST variability provides important implications for North American climate prediction. On the other hand, recent studies also indicate that North American climate is closely correlated with adjacent atmospheric and oceanic anomalies that are not directly attributable to ENSO (e.g., Lin and Wu 2011, 2012; Francis and Vavrus 2012; Wang et al. 2014; Bond et al. 2015; Hartmann 2015; Yu and Zhang 2015; Kug et al. 2015). This suggests that an improved understanding of extratropical atmospheric and oceanic variability is also highly relevant to North American climate prediction.

A recent analysis (Yu et al. 2016) suggested that North American winter temperature variability tends to be dominated by two leading maximum covariance modes of

North American surface temperature and large-scale 500-hPa geopotential height anomalies. Besides the PNA-like structure, the leading mode also shows significant circulation anomalies over Eurasia. An Asian–Bering–North American (ABNA) pattern index was therefore proposed by excluding the PNA influence, which yields a new zonally-elongated teleconnection over the northern extratropics. The first mode is closely related to the PNA and ABNA patterns, and the second mode to the North Atlantic Oscillation (NAO, e.g., Hurrell et al. 2003). Thus North American winter temperature is mostly controlled by these three atmospheric teleconnection patterns. It is noted that stationary Rossby waves, which play an important role in interannual variability of the teleconnections spanning from Eurasia to North America, are observed not only in winter but also in summer (e.g., Schubert et al. 2011; Ding et al. 2011; Wu et al. 2009, 2012). Therefore, this study extends our previous analysis by characterizing the seasonality of the ABNA pattern. In particular, we will explore whether the ABNA teleconnection is a year-round phenomenon and shows peak variability during a certain season.

We then examine the maintenance of the ABNA pattern. Generally, atmospheric circulation anomalies may be driven either by internal atmospheric processes or by external boundary forcings. In the northern extratropics, the maintenance of circulation anomalies mainly includes: (a) the interaction between the time-mean flow and the anomalies, in particular, atmospheric perturbations may grow by extracting energy from the climatological mean flow (e.g., Simmons et al. 1983; Hoskins et al. 1983; Branstator 1995), and (b) transient eddy feedbacks, in particular the synoptic-scale eddy feedback (e.g., Lau 1988; Branstator 1995; Kug and Jin 2009). Extratropical atmospheric circulation anomalies may also be driven by external forcings, in particular SST and diabatic heating anomalies in the tropics, via the resulting planetary circulation anomaly (e.g., Hoskins and Karoly 1981; Hoerling et al. 1997; Trenberth et al. 1998; Branstator 2002; Seager et al. 2003; Ding et al. 2011; Wu and Lin 2012; Yu and Lin 2016). Hence we explore the maintenance of the ABNA pattern by analyzing anomalies in the contribution of synoptic-scale transient eddies on circulation, SST, snow water equivalent, and the surface energy budget to broaden our understanding of the processes that support the circulation and temperature anomalies associated with this teleconnection. In addition, we evaluate the impact of the ABNA pattern on North American climate by analyzing anomalies in North American temperature and temperature extremes explained by this teleconnection. The importance of the ABNA impact on North America is assessed by comparing it with that due to the PNA and NAO.

The paper is organized as follows: the next section describes the data and methods. The seasonality of the ABNA pattern is presented in Sect. 3. Section 4 discusses the maintenance of this teleconnection. Section 5 describes the ABNA impacts on North American temperature and temperature extremes. Results are summarized and further discussed in Sect. 6.

2 Data and methods

The analysis is based on monthly mean atmospheric variables obtained from the National Centers for Environmental Prediction/National Center for Atmospheric Research (NCEP/NCAR) reanalysis (NCEP hereafter, Kistler et al. 2001) over the period from March 1979 to February 2015. The fields we used involve geopotential and wind velocities in the troposphere, and temperature and heat fluxes at the surface. The monthly surface heat fluxes are averaged from daily flux values. The daily winds from the NCEP reanalysis dataset are also employed to compute synoptic eddy vorticity forcing. All these variables are on standard $2.5° \times 2.5°$ grids. Additionally, the SST from the Met Office Hadley Centre, version 1 (HadISST1.1, Rayner et al. 2003) on $1.0° \times 1.0°$ grids for the same period is employed. We also use monthly snow water equivalent (SWE) data, based on a blend of products and represented on a T42 Gaussian grid (about $2.81° \times 2.81°$), for the period from March 1981 to February 2010 (Mudryk et al. 2015). SWE characterizes the hydrological significance of snow cover, and corresponds to the depth of a layer of water that would accumulate if the snowpack in a particular area were to melt. We also use monthly temperature extreme indices, on a $2.5° \times 3.75°$ (latitude–longitude) grid over North America, for the period from March 1979 to February 2010. These extreme indices include the percentage of time when daily maximum (minimum) temperature is greater than its 90th percentile TX90p (TN90p), and the percentage of time when daily maximum (minimum) temperature less than its 10th percentile TX10p (TN10p), according to the HadEX2 dataset (http://www.climdex.org/indices.html, Donat et al. 2013). In addition, the monthly PNA and NAO teleconnection indices were downloaded from the Climate Prediction Center (http://www.cpc.ncep.noaa.gov/data/indices). The two teleconnection patterns and indices were identified from the Rotated Empirical Orthogonal Function (REOF) analysis of monthly mean standardized 500-hPa height anomalies over the northern extratropics (20°–90°N).

To characterize seasonality, winter is defined as December to February (DJF). Other seasons are defined similarly, i.e., spring as March to May (MAM), summer as June to August (JJA) and autumn as September to November (SON). To assess interannual climate variability, seasonal mean anomalies were obtained by removing the mean seasonal cycles and linear trends over the whole period

considered. The relation between a time series of interest and associated spatial fields is quantified through correlation and regression analyses. The statistical significance level of a correlation is assessed by a Student's t-test, assuming one degree of freedom (DOF) per year. In addition, the power spectra of time series are obtained using the Parzen estimator (e.g., von Storch and Zwiers 1999).

To help in understanding the maintenance of the circulation and surface temperature anomalies, the ABNA-associated anomalies of the transient eddy forcing, SST, snow water equivalent and surface energy budget are examined. In the upper troposphere, the synoptic-scale vorticity forcing is crucial in reinforcing the anomalous circulation (e.g., Lau 1988; Branstator 1995; Kug and Jin 2009). The synoptic-scale scale eddy vorticity forcing (F_v), representing the geopotential tendency, can be expressed as,

$$F_v = -f\nabla^{-2}(\nabla \cdot \overline{V'\zeta'}), \tag{1}$$

where f is the Coriolis parameter, V is the wind velocity including zonal and meridional components, and ζ is the relative vorticity. The prime corresponds to the 2–8 days bandpass filtered synoptic perturbation and the bar represents the seasonal average.

The surface energy budget over land takes the following form (e.g., Yu and Boer 2002; Zhang et al. 2011):

$$C_s \partial T_s / \partial t = Rs^d + Rs^u + Rl^d + Rl^u + LH + SH + Fg + Fm, \tag{2}$$

where C_s is the surface layer heat capacity, T_s is the surface (skin) temperature, Rs^d (Rs^u) is the downward (upward) solar radiation across the surface, Rl^d (Rl^u) is the surface downward (upward) infrared radiation, LH (SH) is the latent (sensible) energy exchange across the surface, Fg indicates the ground heat flux, and Fm represents the surface energy flux used for melt. The sign convention is that the fluxes are positive (negative) if they act to warm (cool) the surface temperature.

The impact of an atmospheric teleconnection on North American climate is evaluated by calculating the percentages of North American temperature and temperature extreme variances explained by the teleconnection,

$$P = \frac{\langle \hat{x}^2 \rangle}{\langle \sigma_x^2 \rangle} \times 100\%, \tag{3}$$

where $\hat{x}$ is the anomaly of variable x (i.e., temperature or temperature extreme) regressed upon the standardized pattern index considered, and σ_x the temporal standard deviation of x. The angular brackets represent the spatial average over North America. Similarly, the percentage of Northern Hemisphere geopotential variance explained by a teleconnection pattern can also be estimated following Eq. (3).

3 Seasonality of the ABNA teleconnection

3.1 Definition of the ABNA index

Following the previous study (Yu et al. 2016), the ABNA teleconnection index is defined as follows: (a) constructing the residual seasonal mean geopotential anomalies at 500-hPa (Φ'_{500}) by removing the PNA contribution from the geopotential field by means of linear regressions, (b) normalizing Φ'_{500} at each grid location by its standard deviation (denoted by braces below) and averaging the anomalies over the three regions A (45°–60°N, 80°–110°E), B (50°–80°N, 160°E–150°W), and C (40°–60°N, 100°–70°W), (c) constructing the ABNA series by a linear combination of the three regionally averaged anomalies:

$$\text{ABNA} = \{\Phi'_{500}\}(A) - \{\Phi'_{500}\}(B) + \{\Phi'_{500}\}(C), \tag{4}$$

and (d) standardizing the resulting series as the ABNA index.

Figure 1 (left) shows the ABNA indices in the four seasons. The correlation coefficient between the ABNA in DJF and the ABNA in lagging MAM (leading SON) is 0.59 (0.43), statistically significant at the 5% level. Except those, the timeseries are not significantly correlated with each other. This indicates that the ABNA teleconnection tends to be more stable around the winter. Table 1 further lists the correlations between the ABNA, PNA and NAO pattern indices. ABNA is uncorrelated with PNA by construction and is only weakly correlated with NAO in all seasons.

A power spectrum analysis reveals that, for the ABNA indices in all four seasons, the time series have power spectra weighted toward interannual timescales (Fig. 1, right). The power peaks are at about 3.5 years for DJF and SON, 6.0 years for MAM, and 2.5 years for JJA. However, all the peaks are not significant at the 5% level.

3.2 ABNA patterns

Figure 2 displays the anomalies of large-scale 500-hPa geopotential (Φ_{500}) and North American 2 m temperature (T_{2m}) regressed on the ABNA indices in DJF, MAM, JJA, and SON. The ABNA associated circulation is dominated by anomalies in the northern extratropics. The positive phase of the ABNA pattern exhibits above-average heights over north-central Asia and north-central North America centered between the Great Lakes and Hudson Bay, and below-average heights over the Bering Sea and Strait region. This reflects a zonally oriented wavetrain originating from North Asia and flowing downstream across Bering Sea and Strait towards North America, as illustrated by diagnosis of the stationary wave activity flux (Yu et al. 2016). The ABNA signature is clearly
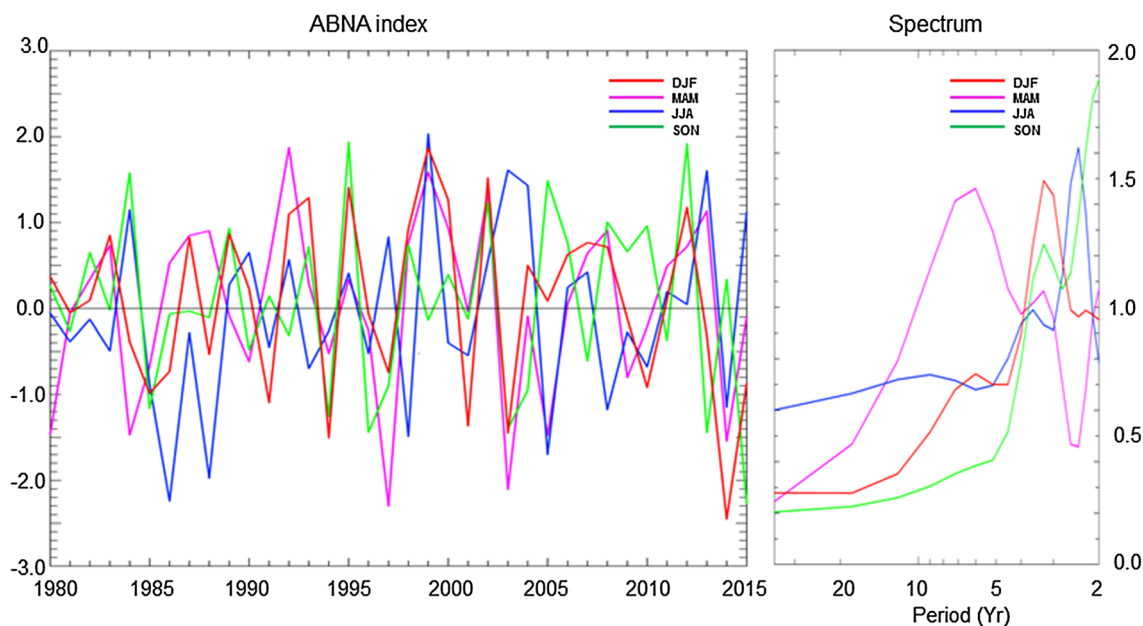
Fig. 1 *Left* the ABNA indices in DJF (*red*), MAM (*magenta*), JJA (*blue*), and SON (*green*). *Right* power spectra for the four time series

Table 1 Correlation coefficients between the teleconnection indices in different seasons

Season corr (x, y)	DJF	MAM	JJA	SON
ABNA, PNA	0.0	0.0	0.0	0.0
ABNA, NAO	0.18	0.10	−0.00	0.12
PNA, NAO	−0.04	−0.21	−0.03	0.03

Assuming one degree of freedom per year, the correlation at the 5% significance level is about 0.33 (for 36 DOF). The ABNA and PNA indices are uncorrelated by construction

detectable in all seasons, but the amplitudes are most substantial in DJF and the weakest in JJA (about half the amplitude of those in DJF). Positive geopotential anomalies are also apparent over the North Pacific and North Atlantic, which are supported by the synoptic eddy forcing as discussed below.

The ABNA associated 500-hPa geopotential anomalies explain about 7–12% of total interannual Φ_{500} variances over the northern extratropics (poleward of 20°N) in the four seasons, calculated following Eq. (3), with the highest value in DJF and the lowest in JJA. By contrast, the PNA (NAO) associated Φ_{500} anomalies explain about 6–14% (10–19%) of total interannual geopotential variances, with the highest value in DJF (DJF) and the lowest in JJA (SON). The percentages of the extratropical Φ_{500} variance explained by the ABNA teleconnection are comparable to the PNA and NAO counterparts, indicating the importance of the ABNA pattern in characterizing the northern extratropical circulation anomalies.

The exchange of midlatitude and polar air following the anomalous circulation, with accompanying temperature advection, plays an important role in establishing and maintaining the anomalous temperature. Hence, in association with the positive phase of the ABNA pattern, T_{2m} tends to exhibit warm anomalies over North Asia and the central-east parts of North America, and cold anomalies around Bering Strait. In particular, over North America, pronounced warm anomalies are apparent over the Great Plains and Great Lakes, accompanied by cold anomalies over Alaska, the western coast of North America, and the extreme northeastern Canada (with an exception in JJA). This indicates the close relation between the ABNA teleconnection and North American temperature variability, as will be examined quantitatively in Sect. 5. Over North Asia, prominent warm anomalies over the West Siberian plain and Central Siberian Plateau accompany the anticyclonic anomaly. Broadly similar patterns of T_{2m} anomalies appear in the four seasons. However, the anomalies are the strongest in DJF and the weakest in JJA, consistent with the seasonal variance of the circulation anomalies.

The ABNA pattern bears some resemblance to the cold ocean–warm land (COWL, Wallace et al. 1996) pattern. The positive phase of the COWL pattern is characterized by above-average heights over Siberia and the Yukon and below-average heights over the Barents Sea and the North Pacific. The two patterns contain similar elements over north Asia and North America, and differences mainly over the oceans. In particular, the ABNA is marked by below-average heights over the Bering Sea and Strait region as

Fig. 2 Anomalies of the tropical and Northern Hemisphere Φ_{500} (contours, interval 60 m^2 s^{-2}) and Northern Hemisphere T$_{2m}$ (*shading*, in °C, over lands poleward of 20°N) regressed upon the ABNA indices in DJF, MAM, JJA, and SON (from the *top* to the *bottom*). Negative geopotential anomalies are *cross-hatched*. The three *black boxes* indicate the areas A (45°–60°N, 80°–110°E), B (50°–80°N, 160°E–150°W), and C (40°–60°N, 100°–70°W) used for constructing the ABNA index
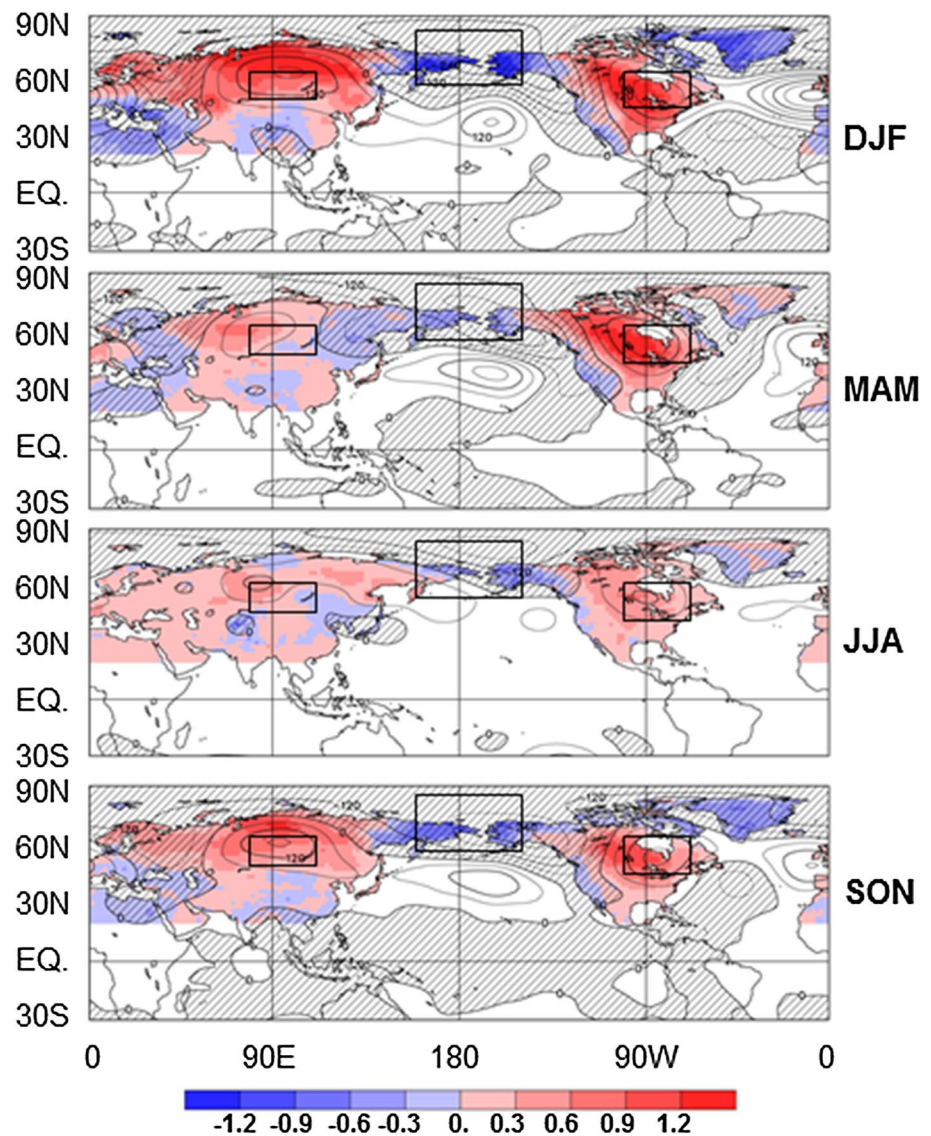
well as relatively weak above-average heights over the North Pacific. In addition, it should be noted that, like the COWL pattern, the ABNA pattern is not a modal structure in its own right. No such pattern appears from the empirical orthogonal function (EOF) analysis of the northern extratropical 500-hPa geopotential field. Nevertheless, it remains to examine if the ABNA would arise from a cluster method, such as k-means clustering or self-organizing maps.

4 Maintenance of the ABNA teleconnection

4.1 Transient eddy contribution

Similar geopotential anomalies in association with the ABNA variability are apparent at 250-hPa and 500-hPa (cf. Fig. 3 with Fig. 2), indicating that the ABNA teleconnection exhibits an equivalent barotropic structure in the troposphere. In the northern mid-high latitudes, the 250-hPa synoptic eddy forcing F_{v250} (contours in Fig. 3) exhibits anticyclonic forcing over north-central North America and north-central Asia, and cyclonic forcing over Bering Sea and Strait and the northeastern Pacific. The centers of action of the eddy forcing anomalies collocate with those of the circulation anomalies (although the anomalous forcing centers are displaced slightly southward compared to the corresponding geopotential centers), implying that synoptic-scale eddies systematically reinforce and help in maintaining the ABNA associated large-scale circulation anomalies. F_{v250} anomalies are stronger in DJF than in JJA, especially over Bering Sea and Strait and North America, resembling the seasonal variation of the Φ_{250} anomalies. In addition, marked synoptic eddy forcing anomalies collocate well with the pronounced geopotential anomalies over the

Fig. 3 Anomalies of Φ_{250} (*shading*, in m^2 s^{-2}) and F_{v250} (*contours*, interval 2.0×10^{-4} m^2 s^{-3}) regressed upon the ABNA indices in DJF, MAM, JJA, and SON (from the *top* to the *bottom*). Negative F_{v250} anomalies are *cross-hatched*
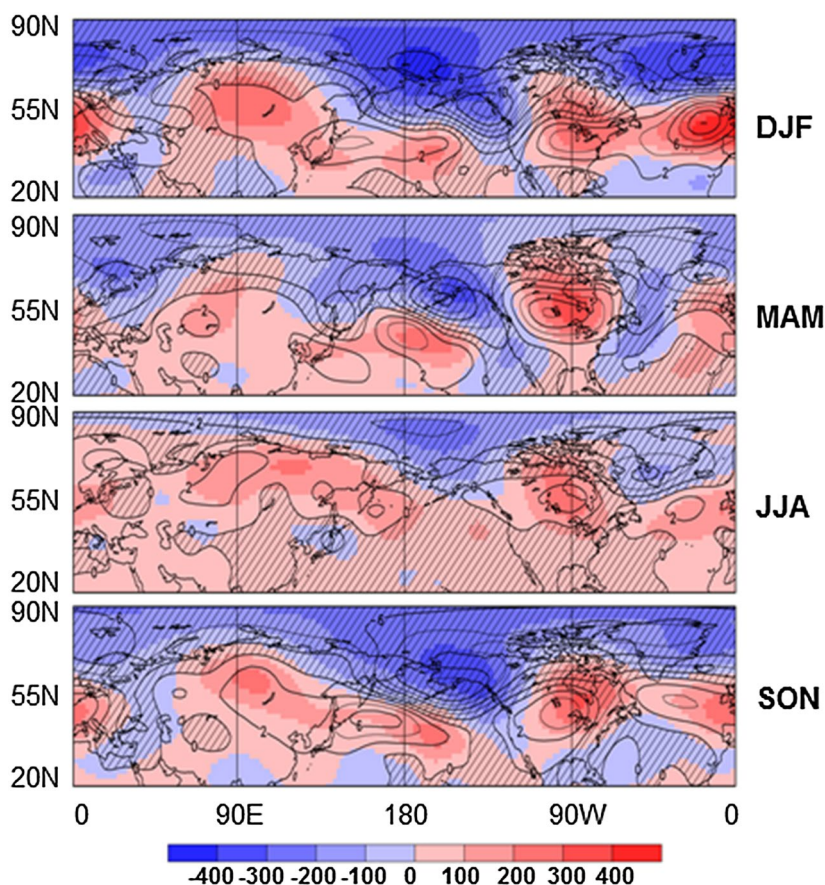

4.2 SST and SWE

Figure 4 displays SST and surface wind anomalies regressed on the ABNA indices. In association with the ABNA pattern, DJF SST shows pronounced anomalies in the mid-high latitudes of North Pacific and North Atlantic (Fig. 4, top panel). In particular, the anomalies exhibit a horseshoe-shaped structure of below-average SSTs in the northeastern and subtropical North Pacific and above-average SSTs in the midlatitude North Pacific. The corresponding circulation anomalies, especially the cyclonic anomaly over Bering Sea and Strait and the relatively weak anticyclonic anomaly in the midlatitude North Pacific (Fig. 2), bring anomalous northwesterly winds over the northeastern Pacific and easterly winds in the midlatitude North Pacific (vectors in Fig. 4). The strongest northwesterly (or easterly) wind anomalies in the North Pacific are well collocated with the dominant action center of below (or above) average SSTs in the northeastern (or midlatitude) Pacific. This suggests that the SST is largely driven by the circulation anomalies in the North Pacific mid-high latitudes,

mainly due to changes in latent and sensible heat fluxes at the ocean surface resulting from the anomalous surface wind (shown in the "Appendix"), as documented in previous studies (e.g., Cayan 1992; Kushnir et al. 2002; Linkin and Nigam 2008). Similar ocean–atmosphere relationship appears in the North Atlantic. In contrast, the ABNA associated SST and surface wind anomalies are generally weak in the tropics. The anomalous SST pattern observed in DJF is also seen in MAM and SON, although the anomalies are weaker in the latter two seasons than in DJF. Additionally, the anomalies are weak and less well organized in JJA, corresponding to the weak circulation anomalies in summer.

Figure 5 shows the ABNA associated snow water equivalent anomalies. Corresponding to the pronounced temperature anomalies in North Asia and North America (Fig. 2), significant SWE anomalies are observed in autumn, winter, and spring, but not in summer as would be expected. In SON, the positive phase of the ABNA pattern is related to a prominent SWE decrease over the West Siberian plain and Central Siberian Plateau in North Asia and over the Great Plains and Great Lakes in North America. The pronounced snow decrease in North Asia shifts southward subsequently and is situated over southern Siberia in midwinter DJF, accompanied by slight SWE increase over the West Siberian plain and Central Siberian Plateau. In MAM,

mid-latitudes of North Pacific and North Atlantic, indicating the synoptic transient eddies reinforce circulation anomalies there as well.

Fig. 4 Regressions of SST (contours 0.1 °C, values greater (less) than 0.1 °C are *red* (*blue shaded*) and 1000-hPa wind (vectors, ms^{-1}) anomalies on the ABNA indices in DJF, MAM, JJA, and SON (from the *top* to the *bottom*). Wind anomalies less than 0.2 ms^{-1} in both directions are omitted. The wind vector scale is shown at the *lower right*
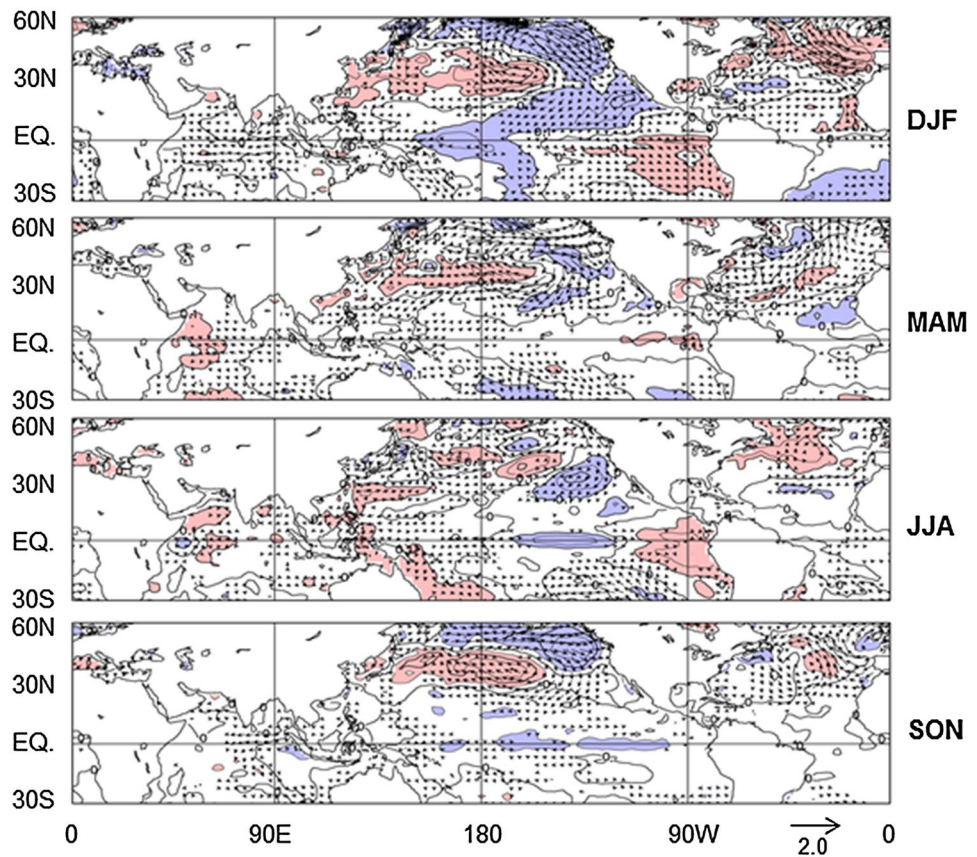
the anomalous SWE center moves back northwards. The pronounced temperature increase (or decrease) collocates with significant snow decrease (or increase) (cf., Fig. 2 with Fig. 5), indicating the positive feedback process of snow–temperature interactions over North Asia and North America. Thus the ABNA associated variations of SWE, temperature and circulation suggest potential snow forcing influences on the variations of surface temperature and atmospheric circulation from autumn to spring, via changes in the surface energy budget, as demonstrated in previous studies (e.g., Cohen and Entekhabi 1999; Saito and Cohen 2003; Goddard et al. 2006; Wang et al. 2010; Lin and Wu 2011). Nevertheless, the slight SWE increase over the West Siberian plain and Central Siberian Plateau in DJF, with accompanying surface temperature increase, indicates that the snow fluctuations in those areas may also be the consequence of variations in large-scale circulation and temperature in winter, the process as documented in some other studies (e.g., Walsh et al. 1982; Clark and Serreze 2000).

Figure 6 further shows the SON (DJF) SWE anomalies regressed upon the DJF (MAM) ABNA index, with anomalous snow leading the atmospheric pattern by one season. It is interesting that the simultaneous snow anomalies associated with the ABNA indices in DJF and MAM (Fig. 5) are also apparent in the corresponding SWE anomalies one

season before, in particular for the anomalies over North Asia. This suggests a snow forcing influence on the ABNA pattern in winter and spring that can be traced back to the preceding season, which makes it of seasonal climate prediction value. The result is also in agreement with Lin and Wu (2011), which investigated the relationship between the snow cover variations over Siberia and the Tibetan Plateau and large-scale circulation anomalies over North Asia and its impact on North American winter temperature. By contrast, the one season lead SWE anomalies are weak in the other two seasons (not shown).

4.3 Surface energy budget

In association with the ABNA pattern, the surface energy budget is dominated by variations in surface longwave radiations (Fig. 7), which correspond closely with surface temperature anomalies (Fig. 2). In particular, the anomalous downward surface longwave radiation Rl^d tends to support the ABNA associated temperature anomalies while the upward longwave radiation Rl^u damps the temperature anomalies. Over North America and North Asia, there is more downwelling longwave radiation at the warm surface, which is offset by the increase of outgoing longwave radiation. This is a straightforward consequence of the

Fig. 5 Regressions of snow water equivalent (*contours*, interval 0.2 cm) anomalies on the ABNA indices in DJF, MAM, JJA, and SON (from the *top* to the *bottom*). The positive (negative) anomalies significantly correlated with the ABNA index at the 5% level are *red* (*blue*) *shaded*. Negative anomalies are *cross-hatched*
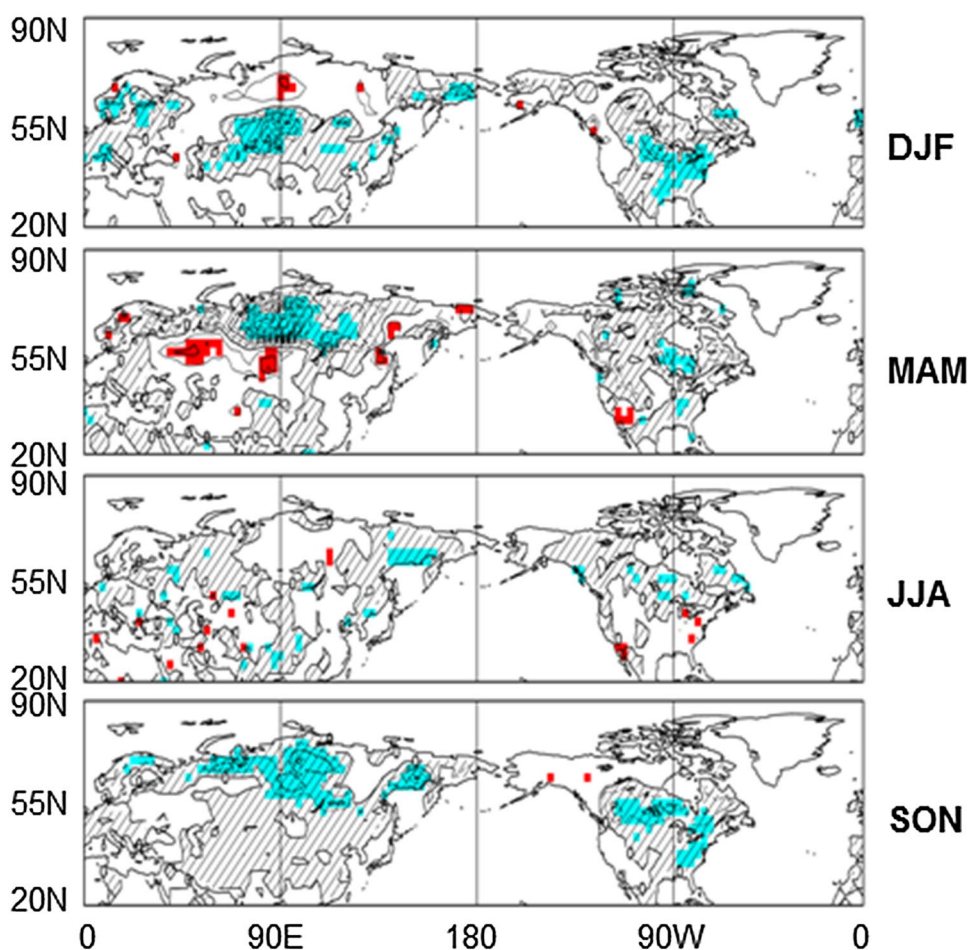
Fig. 6 (*Top*) SON snow water equivalent anomalies regressed upon the DJF ABNA index. (*Bottom*) DJF snow water equivalent anomalies regressed upon the MAM ABNA index. The contour interval is 0.2 cm. The positive (negative) anomalies significantly correlated with the ABNA index at the 5% level are *red* (*blue*) *shaded*. Negative anomalies are *cross-hatched*
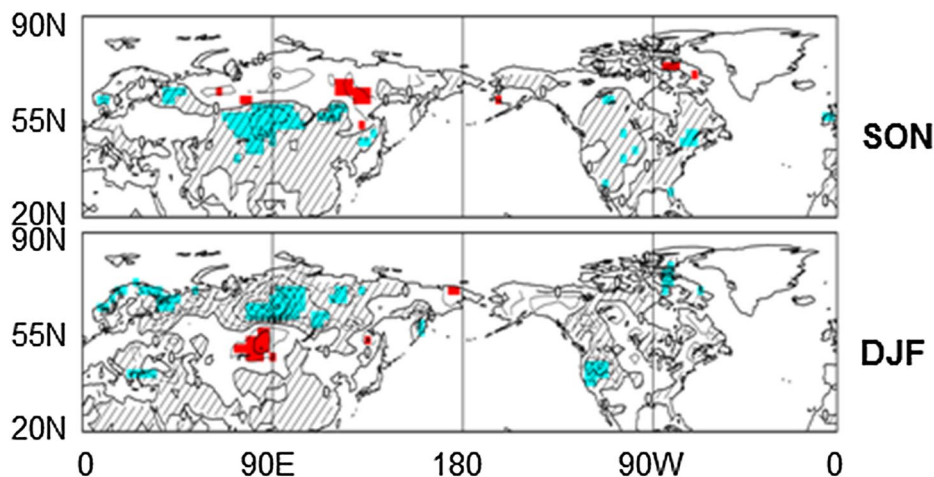
Planck feedback (e.g., Peixoto and Oort 1992). However, it remains to explore if the downwelling longwave radiation anomaly is due to anomalous thermal advection and/or anomalies in water vapor and clouds, the two factors highlighted recently by Gong et al. (2017) in investigating the increase in the Arctic surface air temperature. The ABNA associated surface shortwave radiation anomalies are weak (not shown). The anomalous net surface radiation, the sum of surface longwave and shortwave radiations, is a small residual mainly from the cancellation of Rl^d and Rl^u anomalies.

The ABNA associated surface latent heat flux LH anomalies are weak, while its associated sensible heat flux SH pattern bears some resemblance to the Rl^d
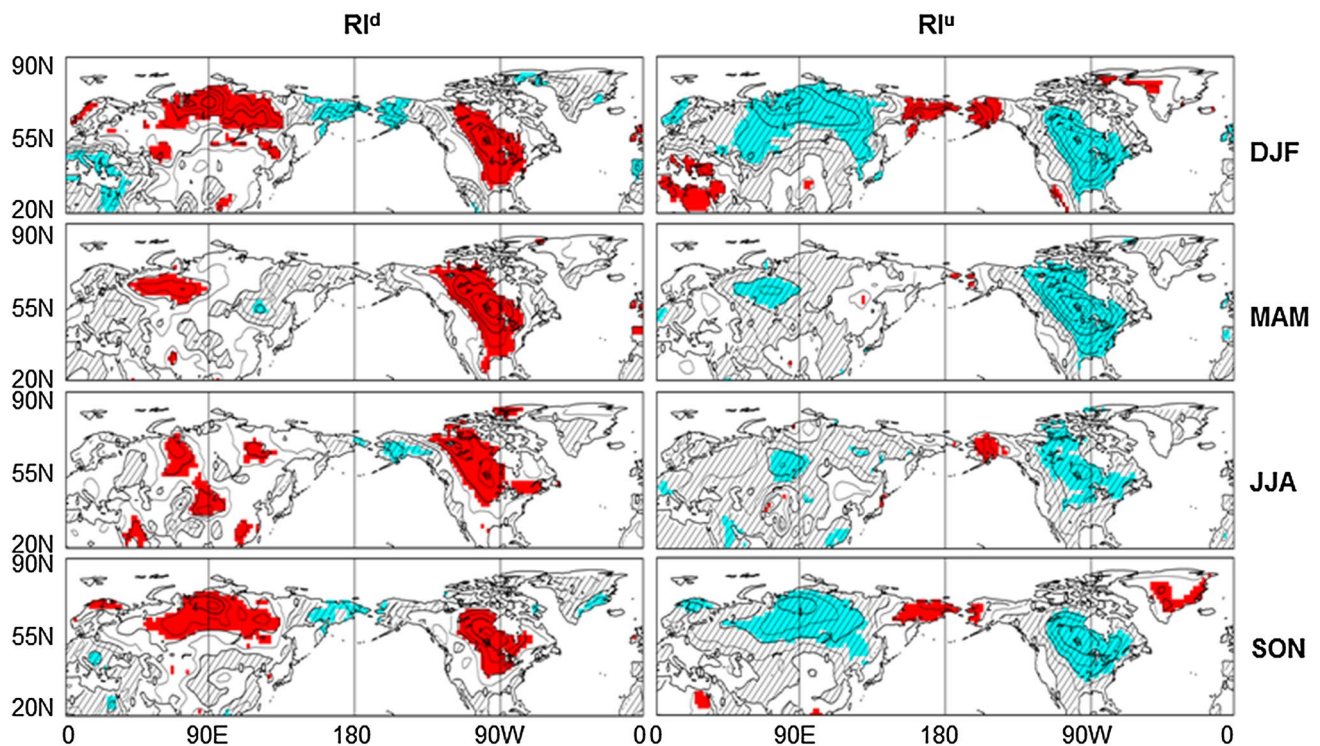
Fig. 7 Anomalies of downward longwave radiation Rl^d (*left column*) and upward longwave radiation Rl^u (*right column*) regressed upon the ABNA indices in DJF, MAM, JJA, and SON (from the *top* to the *bottom*). The contour interval is 1.0 W m^{-2}. The positive (negative) anomalies significantly correlated with the ABNA index at the 5% level are *red* (*blue*) *shaded*. Negative anomalies are *cross-hatched*

pattern and the *SH* anomalies are about 1/3–1/2 times the amplitude of those in *Rl^d* anomalies (not shown). The anomalous sensible heat flux is positively correlated with surface temperature, corresponding to the atmosphere warming the surface, while the latent heat flux anomaly is negatively correlated, corresponding to latent cooling due to increased evaporation and sublimation in the presence of warm anomalies. In addition, the anomalous *Fg* and *Fm* fluxes in Eq. (2) are small and negligible (not shown). Hence, in general, the sensible heat flux anomalies compensate the net surface radiative anomalies.

Broadly similar surface energy budget features are seen in the four seasons, although the heat flux anomalies are the most substantial in winter and the least in summer, consistent with the seasonal variation of surface temperature anomalies in Fig. 2. Thus, in association with the positive (or negative) ABNA phase, it is warmer (or colder) in North America and North Asia, while the surface equilibrates with the warm (or cold) air by enhanced (or reduced) thermal radiation between the ground and the air.

5 ABNA impacts on North American temperature and temperature extremes

5.1 Surface temperature

Figure 8 presents the interannual variance of North American T$_{2m}$ (left column) and T$_{2m}$ anomalies regressed upon the ABNA, PNA, and NAO indices (right columns). North American temperature shows considerable interannual and interseasonal variability. It tends to be characterized by high variances over a northwest–southeast belt extending from Alaska towards the southeastern US, with large anomalies over the Canadian Prairie and the Canadian Shield. The temperature variance is strongest in winter and weakest in summer.

As described in Sect. 3.2, the positive phase of the ABNA pattern is dominated by above-average temperatures over the central-eastern parts of North America, with pronounced warm anomalies over the Great Plains and Great Lakes, accompanied by cold anomalies over Alaska, the western coast of North America, and extreme northeastern Canada (with the exception of JJA). Most prominent
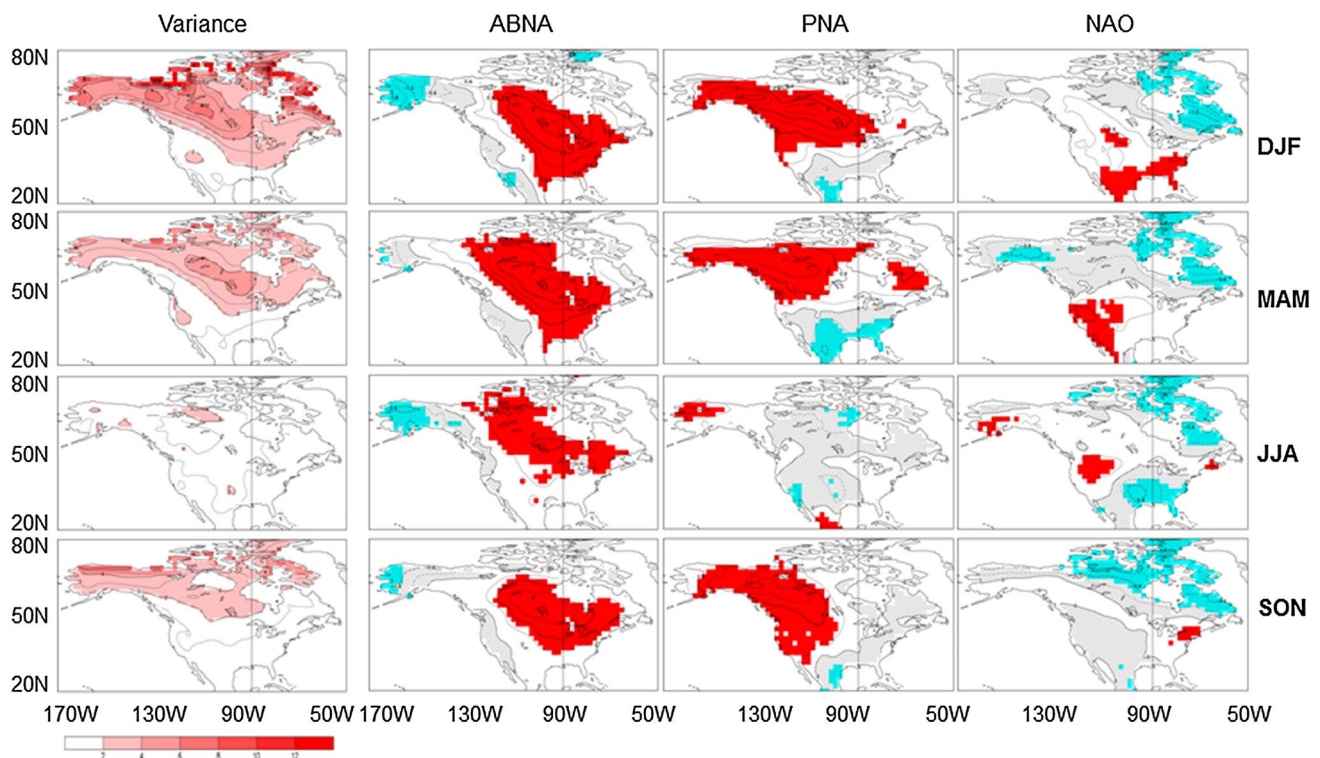
Fig. 8 (*Left column*) Variances of North American T_{2m} (*contours and shading*, interval 1.0 °C^2). (*Right column 2–4*) Regressions of T_{2m} (*contours*, interval 0.3 °C) anomalies on the ABNA, PNA, and NAO indices. The positive (negative) anomalies significantly cor-related with the ABNA index at the 5% level are *red* (*blue*) *shaded*. Negative anomalies are *cross-hatched*. Results for DJF, MAM, JJA, and SON are shown from the *top* to the *bottom rows*

Table 2 Percentages of North American T_{2m} variance explained by the teleconnections in different seasons

Season index	DJF	MAM	JJA	SON
ABNA	17.8	20.5	9.8	13.4
PNA	15.0	11.5	3.9	12.6
NAO	9.0	9.2	7.4	10.0

The results are estimated over the lands within (20°–80°N, 170°–50°W), excluding Greenland

anomalies are situated over high temperature variance areas. Similar patterns of T_{2m} anomalies are seen in the four seasons. Yet the anomalies are the strongest (or weakest) in DJF (or JJA), with the highest values reaching 1.6 °C (or 0.7 °C) around the Great Lakes. The relationship between the ABNA pattern and the North American temperature variability may be quantified by calculating the percentage of the North American temperature variance explained by the teleconnection, following Eq. (3), over the land areas within (20°–80°N, 170°–50°W). Table 2 lists the results. The ABNA associated temperature anomalies explain about 15–20% of total interannual T_{2m} variances in winter, spring and autumn, and about 10% in summer.

As documented in previous studies (e.g., Barnston and Livezey 1987; Barlow et al. 2001; Higgins et al. 2002; Yu and Zwiers 2007), the positive phase of the PNA pattern is related to above-average temperatures over western Canada and the northwestern US, as well as below-average temperatures across the south-central and southeastern US in DJF, MAM and SON (Fig. 8, 3rd column). The PNA has little impact on North American temperature variability during summer. The PNA associated temperature anomalies explain about 10–15% of total T_{2m} variances in winter, spring and autumn, and less than 5% in summer (Table 2). In addition, the positive phase of the NAO is accompanied by below-average temperatures in northeastern Canada in all seasons (Fig. 8, right column), in agreement with previous studies (e.g., von Loon and Rogers 1978; Hurrell 1996; Marshall et al. 2001), but above-average temperatures in different areas during various seasons. The NAO associated temperature anomalies explain about 10% of total T_{2m} variances in the four seasons.

The percentages of the North American temperature variance explained by the ABNA and PNA teleconnections are comparable in all seasons, with higher values for ABNA especially in JJA and MAM, and are higher than the NAO counterparts (with the exception of PNA in summer). This

suggests that, besides the PNA and NAO impacts, North American temperature is also significantly controlled by the ABNA pattern in all seasons, consistent with the DJF result reported in Yu et al. (2016).

It is interesting that the relationship between the ABNA and North American temperature variability is also apparent in two ABNA extreme cases. The positive (or negative) extreme value of the ABNA index in DJF appears in the 1998/1999 (or 2013/2014) winter (Fig. 1), which corresponds well to significant warm (or cold) anomalies over North America. As documented in previous studies (e.g., Bell et al. 2000), surface temperatures in the northern extratropics were the second warmest in the historical record during 1999, over the period 1880–2000 considered, including pronounced warm anomalies over North America. However, the 1998/1999 winter was associated with Pacific cold episode (La Niña) with significant cooling in the tropical Pacific. The relationship between the tropical SST and North American temperature for this winter is in contrast with the mean climate impact associated with tropical ENSO events (e.g., Ropelewski and Halpert 1986; Halpert and Ropelewski 1992). In addition, the winter of 2013/2014 featured severe cold anomalies over North America and was accompanied by weak SST anomalies in the tropical Pacific (e.g., Bond et al. 2015; Hartmann 2015;

Yu and Zhang 2015). The tropical SST thus did not play a major role in North American temperature anomalies in these two winters.

5.2 Temperature extremes

Figure 9 displays the interannual variances of extreme indices of warm days TX90p, warm nights TN90p, cool days TX10p and cool nights TN10p in the four seasons. Figure 10 shows the corresponding anomalies of these temperature extreme indices regressed upon the ABNA indices.

The variance of warm days TX90p (Fig. 9, left column) is comparable in the four seasons and tends to exhibit high values over Alaska, extreme northern Canada over the Central and East Arctic areas, the Colorado Plateau and Great Basin, and around the Great Lakes. High variance is also apparent in the southeastern US in summer. The positive phase of the ABNA features increased warm days over the Great Plains and Great Lakes, accompanied by reductions over Alaska and the west coast of North America (Fig. 10, left column). The anomalous TX90p patterns bear some resemblance to the corresponding mean surface temperature patterns (Fig. 8). The ABNA associated warm day anomalies explain about 6–9% of total interannual TX90p variance over North America in the four seasons. The
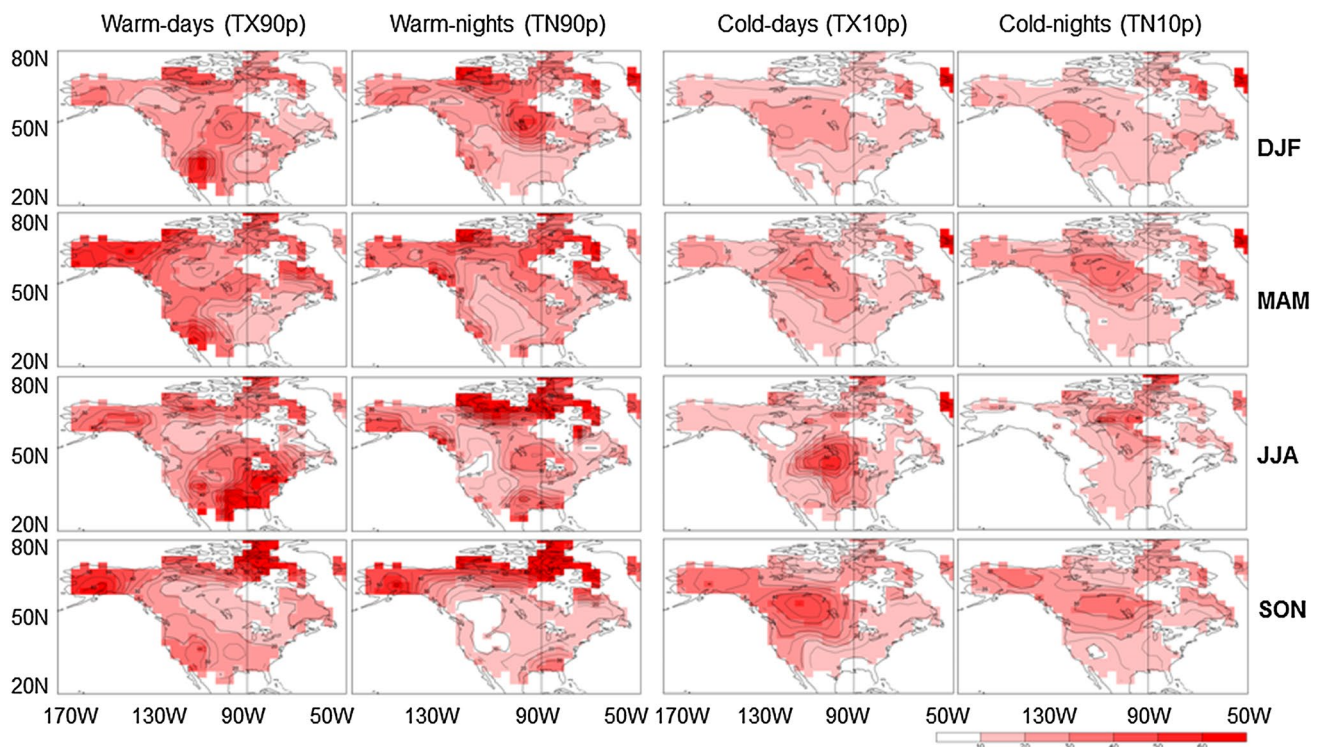
Fig. 9 Variances of North American climate extreme (*contours* and *shading*, interval 5.0%^{2}) in DJF, MAM, JJA, and SON (from the *top* to the *bottom rows*). Anomalies of percentages of warm days (TX90p), warm nights (TN90p), cold days (TX10p), and cold nights (TN10p) are shown from the *left* to the *right columns*
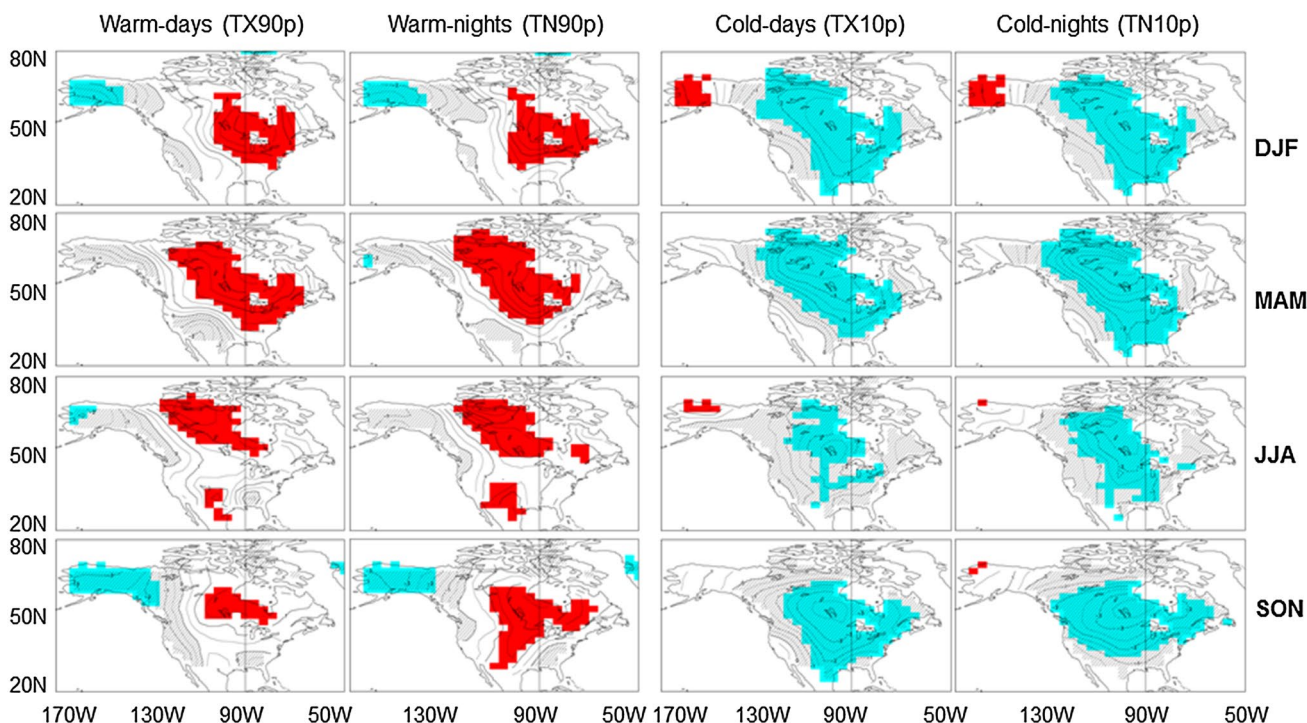
Fig. 10 Regressions of North American climate extreme (*contours*, interval 0.5%) anomalies on the ABNA indices in DJF, MAM, JJA, and SON (from the *top* to the *bottom rows*). Anomalies of percentages of warm days (TX90p), warm nights (TN90p), cold days (TX10p), and cold nights (TN10p) are shown from the *left* to the *right columns*. The positive (negative) anomalies significantly correlated with the ABNA index at the 5% level are *red* (*blue*) *shaded*. Negative anomalies are *cross-hatched*

Table 3 Percentages of North American temperature extreme variances explained by the teleconnections in different seasons

Season		DJF	MAM	JJA	SON
Extreme	Index				
TX90p	ABNA	8.9	9.1	6.5	6.0
	PNA	10.9	10.2	6.1	9.2
	NAO	3.2	12.7	6.8	10.6
TN90p	ABNA	9.3	10.1	8.5	9.2
	PNA	17.2	14.8	4.9	7.8
	NAO	3.1	12.3	8.3	16.6
TX10p	ABNA	17.5	18.7	8.0	14.6
	PNA	22.3	10.9	4.6	14.4
	NAO	4.8	6.7	4.3	4.7
TN10p	ABNA	16.3	23.0	11.5	16.5
	PNA	22.1	12.5	6.5	12.1
	NAO	5.1	7.9	4.1	8.2

The results are estimated over the lands within (20°–80°N, 170°–50°W)

percentages are comparable to those explained by the PNA and NAO patterns (Table 3).

The variance of warm nights TN90p (Fig. 9, 2nd column) bears some resemblance to the corresponding TX90p variance, especially in the northern portions over North America. However, the TN90p variance is generally weaker over Colorado Plateau and Great Basin than the TX90p counterpart. Similarities are also evident in the corresponding TN90p and TX90p anomalies in association with the ABNA pattern (cf. 2nd column with 1st column of Fig. 10), with slight differences mainly in amplitude. The ABNA associated warm night anomalies explain about 10% of total TN90p variance over North America in the four seasons (Table 3). The percentages are comparable to the PNA counterparts, lower (or higher) than the PNA counterparts in DJF and MAM (or JJA and SON), and are also comparable to those explained by the NAO teleconnection (Table 3).

The variance of cold days TX10p (Fig. 9, 3rd column) tends to exhibit high values over the western-central parts of south Canada and the northern US The variance is the weakest in DJF and strongest in JJA, indicating the high interannual TX10p variation in summer. The variances of cold nights TN10p (Fig. 9, right column) bear resemblance to the corresponding TX10p variances, except that in JJA during which the high variance center shifts to north Canada. The positive phase of the ABNA is related to reduced cold days and cold nights over most parts of North America, especially those over the Great Plains and

Great Lakes, accompanied by some increased cold anomalies over Alaska (Fig. 10, right two columns). The ABNA associated TX10p and TN10p anomalies explain about 10–20% of their total interannual variances over North America (Table 3). The percentages are comparable to those explained by the PNA pattern and are higher than the NAO counterparts (about 4–8%).

6 Summary and discussion

The seasonality, maintenance and climate impact of the ABNA teleconnection have been studied using the NCEP reanalysis data for the period from 1979 to 2015 and observation based SST, snow water equivalent and temperature extreme datasets. Following our previous study (Yu et al. 2016), the ABNA index is constructed from the normalized 500-hPa geopotential heights by excluding the PNA pattern influence. The positive phase of the ABNA pattern exhibits above-average heights located in north-central Asia and north-central North America, centered between the Great Lakes and Hudson Bay, as well as below-average heights located over Bering Sea and Strait. It reflects a zonally elongated wavetrain originating from North Asia and flowing downstream towards North America. As the consequence of the anomalous circulation imposed by anomalous thermal advection, near-surface temperatures tend to exhibit warm anomalies over North Asia and the central-eastern parts of North America, accompanied by cold anomalies around the Bering Strait. The ABNA signature is clearly detectable year-around, but the amplitudes are most substantial in winter and the least in summer.

The ABNA pattern has an equivalent barotropic structure in the troposphere. The anomalous circulation is sustained by synoptic eddy forcing in the upper troposphere. The positive phase of the ABNA pattern is associated with a horseshoe-shaped structure of below-average SSTs in the northeastern and subtropical North Pacific and above-average SSTs in the midlatitude North Pacific. The SST structure is most prominent in winter and less well organized in summer. The SST is driven by the circulation anomalies in the North Pacific and North Atlantic mid-high latitudes.

The snow cover anomalies over the West Siberian plain and Central Siberian Plateau in autumn and spring and over southern Siberia in winter may act as a forcing influence on the ABNA teleconnection. Moreover, the snow forcing influence on the ABNA pattern in winter and spring can be traced back to the preceding season, which provides a predictability source for this teleconnection and hence North American temperature variability. The ABNA associated energy budget is dominated by the surface longwave radiation anomalies year-round, as the consequence of the anomalous advection. When it is warmer (colder) in North Asia and North America, the surface equilibrates with the warm (cold) air mainly by enhanced (reduced) thermal radiation between the ground and the air.

North American surface temperature and temperature extremes exhibit considerable interannual and interseasonal variability. The ABNA associated anomalies explain about 15–20% of total interannual surface temperature variance over North America in winter, spring and autumn, and close to 10% in summer. The explained percentages are slightly higher than the PNA counterparts and are much higher than those explained by the NAO pattern. The positive (or negative) extreme value of the ABNA index in the 1998/1999 (or 2013/2014) winter is also found to correspond to significant warm (or cold) anomalies over North America. Thus, besides the PNA and NAO impacts, North American temperature is also significantly controlled by the ABNA teleconnection. In addition, the ABNA associated warm day and warm night (or cold day and cold night) anomalies explain about 5–10% (or 10–20%) of the corresponding total variances over North America, which are comparable to the PNA and NAO associated counterparts as well. Mechanisms causing the changes in temperature extremes remain to be explored.

The centers of action of the ABNA teleconnection are situated in the northern mid-high latitudes, away from the subtropical-midlatitude jet stream. Hence the generation of this zonally-oriented wavetrain is not closely related to local processes of jet instabilities (e.g., Simmons et al. 1983; Wallace and Lau 1985). Analysis of the ABNA associated zonal wind and kinetic energy anomalies confirms this and reveals that the barotropic instability of the mean flow does not play an important role in sustaining the ABNA teleconnection. Results from the ABNA associated snow water equivalent anomalies are also obtained from the snow cover field (not shown). Nevertheless, other forcing influences, such as sea ice cover in the Arctic (e.g., Cohen et al. 2014; Nakanowatari et al. 2015), on the ABNA pattern remain to be examined. In addition, whether the ABNA coexists with other atmospheric teleconnections, such as the Arctic Oscillation (AO, Thompson and Wallace 1998), the circumglobal teleconnection (CGT, Branstator 2002; Ding et al. 2011), and the Western Pacific index (Wallace and Gutzler 1981) that is significantly correlated with the ABNA index in winter (Yu et al. 2016), in a certain season or year-round, and the degree to which these phenomena are interrelated have yet to be explored.

Appendix

ABNA associated surface energy budget over ocean.

The surface energy budget over ocean can be written as (e.g., Yu and Boer 2002),

$$C_* \partial T_s / \partial t = Rl + Rs + LH + SH + A, \qquad (5)$$

where C_* is the effective heat capacity of the surface layer, T_s the surface temperature, Rl (Rs) the longwave (shortwave) radiation across the surface, and LH (SH) the latent (sensible) heat flux exchanges across the surface. A is the convergence of heat into the surface layer by oceanic transport and is obtained as a residual in the equation. Note that all fluxes are defined positive downward, i.e. in the direction so as to increase T_s. For the steady state (such as seasonal means in this study) and not the evolution, the left-hand side of Eq. (5) is much smaller than all other terms in the equation and is not considered. The ABNA associated flux anomalies in DJF are shown in Fig. 11. Results indicate that the anomalous LH and SH (because of the anomalous surface wind) tend to support the ABNA associated SST anomalies while the oceanic transport damps the SST anomalies. Broadly similar features are seen in the four seasons.
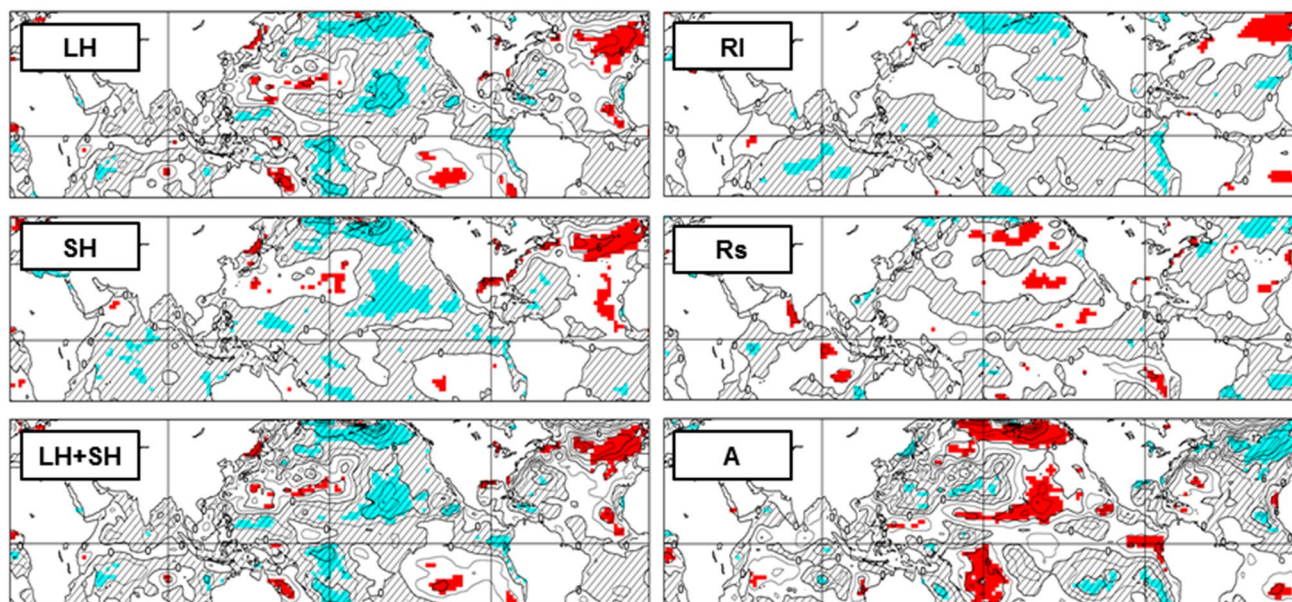
Fig. 11 Anomalies of latent LH (sensible SH) energy exchange across the surface, surface longwave (Rl) and shortwave (Rs) radiation, and oceanic transport (A) regressed upon the ABNA index in DJF. The contour interval is 3.0 W m^{-2}. The positive (negative) anomalies significantly correlated with the ABNA index at the 5% level are *red* (*blue*) *shaded*. Negative anomalies are *cross-hatched*

References

Barlow M, Nigam S, Berbery EH (2001) ENSO, Pacific decadal variability, and US summertime precipitation, drought, and stream flow. J Clim 14:2105–2128

Barnston AG, Livezey RE (1987) Classification, seasonality and persistence of low-frequency atmospheric circulation patterns. Mon Wea Rev 115:1083–1126

Bell GD et al (2000) Climate assessment for 1998. Bull Am Meteorol Soc 81(6):S1–S50

Bond NA, Cronin MF, Freeland H, Mantua N (2015) Causes and impacts of the 2014 warm anomaly in the NE Pacific. Geophys Res Lett 42:3414–3420. doi:10.1002/2015GL063306

Branstator G (1995) Organization of storm track anomalies by recurring low-frequency circulation anomalies. J Atmos Sci 52:207–226

Branstator G (2002) Circumglobal teleconnections, the jet stream waveguide, and the North Atlantic Oscillation. J Clim 15:1893–1910

Cayan DR (1992) Latent and sensible heat flux anomalies over the northern oceans: the connection to monthly atmospheric circulation. J Clim 5:354–369

Clark MP, Serreze MC (2000) Effects of variations in East Asian snow cover on modulating atmospheric circulation over the North Pacific Ocean. J Clim 13:3700–3710

Cohen J, Entekhabi D (1999) Eurasian snow cover variability and Northern Hemisphere climate predictability. Geophys Res Lett 26:345–348

Cohen J et al (2014) Recent Arctic amplification and extreme midlatitude weather. Nat Geosci 7:627–637

Ding Q, Wang B, Wallace JM, Branstator G (2011) Tropical–extratropical teleconnections in boreal summer: observed interannual variability. J Clim 24:1878–1896

Donat MG et al (2013) Updated analyses of temperature and precipitation extreme indices since the beginning of the twentieth century: the HadEX2 dataset. J Geophys Res Atmos 118:2098–2118

Francis JA, Vavrus SJ (2012) Evidence linking Arctic amplification to extreme weather in mid-latitudes. Geophys Res Lett 39:L06801. doi:10.1029/2012GL051000

Goddard L, Kumar A, Hoerling MP, Barnston AG (2006) Diagnosis of anomalous winter temperature over the eastern United Sates during the 2002/03 El Nino. J Clim 19:5624–5636

Gong T, Feldstein SB, Lee S (2017) The role of downward infrared radiation in the recent Arctic winter warming trend. J Clim. doi:10.1175/JCLI-D-16-0180.1

Halpert MS, Ropelewski CF (1992) Surface temperature patterns associated with the Southern Oscillation. J Clim 5:577–593

Hartmann DL (2015) Pacific sea surface temperature and the winter of 2014. Geophys Res Lett 42(6):1894–1902

Higgins RW, Leetmaa A, Kousky VE (2002) Relationships between climate variability and winter temperature extremes in the United States. J Clim 15:1555–1572

Hoerling MP, Kumar A, Zhong M (1997) El Niño, La Niña, and the nonlinearity of their teleconnections. J Clim 10:1769–1786

Hoskins BJ, James IN, White GH (1983) The shape, propagation and mean-flow interaction of large-scale weather systems. J Atmos Sci 40:1595–1612

Hoskins BJ, Karoly DJ (1981) The steady linear response of a spherical atmosphere to thermal and orographic forcing. J Atmos Sci 38:1179–1196

Hurrell JW (1996) Influence of variations in extratropical wintertime teleconnections on Northern Hemisphere temperatures. Geophys Res Lett 23:665–668

Hurrell JW, Kushnir Y, Visbeck M, Ottersen G (2003) An overview of the North Atlantic Oscillation. The North Atlantic Oscillation: climate significance and environmental impact. Geophys Monogr Ser 134:1–35

Kistler R et al (2001) The NCEP-NCAR 50-year reanalysis: monthly means CD-ROM and documentation. Bull Am Meteorol Soc 82:247–268

Kug JS, Jin FF (2009) Left-hand rule for synoptic eddy feedback on low-frequency flow. Geophys Res Lett 36:L05709. doi:10.1029/2008GL036435

Kug JS, Jeong JH, Jang YS, Kim BM, Folland CK, Min SK, Son SW (2015) Two distinct influences of Arctic warming on cold winters over North America and East Asia. Nat Geosci 8:759–762. doi:10.1038/ngeo2517

Kushnir Y, Robinson WA, Bladé I, Hall NMJ, Peng S, Sutton R (2002) Atmospheric GCM response to extratropical SST anomalies: synthesis and evaluation. J Clim 15:2233–2256

Lau NC (1988) Variability of the observed midlatitude storm tracks in relation to the low-frequency changes in the circulation pattern. J Atmos Sci 45:2718–2743

Lin H, Wu ZW (2011) Contribution of the autumn Tibetan Plateau snow cover to seasonal prediction of North American winter temperature. J Clim 24:2801–2813

Lin H, Wu ZW (2012) Contribution of Tibetan Plateau snow cover to the extreme winter conditions of 2009/10. Atmos Ocean 50:86–94

Linkin ME, Nigam S (2008) The North Pacific Oscillation–West Pacific teleconnection pattern: mature-phase structure and winter impacts. J Clim 21:1979–1997

Liu Z, Alexander M (2007) Atmospheric bridge, oceanic tunnel, and global climatic teleconnections. Rev Geophys 45:RG2005. doi:10.1029/2005RG000172

Marshall J, Johnson H, Goodman J (2001) A study of the interaction of the North Atlantic Oscillation with ocean circulation. J Clim 14:1399–1421

Mudryk LR, Derksen C, Kushner PJ, Brown R (2015) Characterization of Northern Hemisphere snow water equivalent datasets, 1981–2010. J Clim 28:8037–8051

Nakanowatari T, Inoue J, Sato K, Kikuchi T (2015) Summer time atmosphere–ocean preconditionings for the Bering Sea ice retreat and the following severe winters in North America. Environ Res Lett 10:094023

Peixoto J, Oort A (1992) The physics of climate. AIP, New York

Rayner NA, Parker DE, Horton EB, Folland CK, Alexander LV, Rowell DP, Kent EC, Kaplan A (2003) Global analyses of sea surface temperature, sea ice, and night marine air temperature since the late nineteenth century. J Geophys Res 108(D14):4407. doi:10.1029/2002JD002670

Ropelewski CF, Halpert MS (1986) North American Precipitation and temperature patterns associated with the El Niño/Southern Oscillation (ENSO). Mon Wea Rev 114:2352–2362

Saito K, Cohen J (2003) The potential role of snow cover in forcing interannual variability of the major Northern Hemisphere mode. Geophys Res Lett 30:1302. doi:10.1029/2002GL016341

Schubert S, Wang H, Suarez M (2011) Warm season subseasonal variability and climate extremes in the Northern Hemisphere: the role of stationary Rossby waves. J Clim 24:4773–4792. doi:10.1175/JCLI-D-10-05035.1

Seager R, Harnik N, Kushnir Y, Robinson W, Miller J (2003) Mechanisms of hemispherically symmetric climate variability. J Clim 16:2960–2978

Simmons AJ, Wallace JM, Branstator GW (1983) Barotropic wave propagation and instability, and atmospheric teleconnection patterns. J Atmos Sci 40:1363–1392

Thompson DWJ, Wallace JM (1998) The Arctic Oscillation signature in wintertime geopotential height and temperature fields. Geophys Res Lett 25:1297–1300

Trenberth KE, Branstator G, Karoly D, Kumar A, Lau NC, Ropelewski C (1998) Progress during TOGA in understanding and modeling global teleconnections associated with tropical sea surface temperatures. J Geophys Res 103:14291–14324

Van Loon H, Rogers JC (1978) The seesaw in winter temperatures between Greenland and Northern Europe. Part I: general description. Mon Wea Rev 106:296–310

Von Storch H, Zwiers FW (1999) Statistical analysis in climate research. Cambridge University Press, Cambridge, p 484

Wallace JM, Gutzler DS (1981) Teleconnections in the geopotential height field during the Northern Hemisphere Winter. Mon Wea Rev 109:784–812

Wallace JM, Lau NC (1985) On the role of barotropic energy conversion in the general circulation. Adv Geophys 28A:33–74

Wallace JM, Zhang Y, Bajuk L (1996) Interpretation of interdecadal trends in Northern Hemisphere surface air temperature. J Clim 9:249–259

Walsh JE, Tucek DR, Peterson MR (1982) Seasonal snow cover and short term climatic fluctuations over the United States. Mon Wea Rev 110:1474–1485

Wang B, Wu ZW, Liu J, Chang CP, Li J, Zhou TJ (2010) Another look at climate variations of the East Asian winter monsoon: Northern and southern temperature modes. J Clim 23:1495–1512

Wang SY, Hipps L, Gillies RR, Yoon JH (2014) Probable causes of the abnormal ridge accompanying the 2013–2014 California drought: ENSO precursor and anthropogenic warming footprint, Geophys Res Lett 41:3220–3226. doi:10.1002/2014GL059748

Wu Z, Lin H (2012) Interdecadal Variability of the ENSO-North Atlantic Oscillation connection in boreal summer. Q J R Meteorol Soc 138:1668–1675

Wu Z, Wang B, Li J, Jin FF (2009) An empirical seasonal prediction model of the East Asian summer monsoon using ENSO and NAO. J Geophys Res 114:D18120. doi:10.1029/2009JD011733

Wu Z, Lin H, Li J, Jiang Z, Ma T (2012) Heat wave frequency variability over North America: two distinct leading modes. J Geophys Res 117:D02102. doi:10.1029/2011JD016908

Yu B, Boer GJ (2002) The roles of radiation and dynamical processes in the El Niño-like response to global warming. Clim Dyn 19:539–553

Yu B, Lin H (2016) Tropical atmospheric forcing of the wintertime North Atlantic Oscillation. J Clim 29:1755–1772. doi:10.1175/JCLI-D-15-0583.1

Yu B, Zhang X (2015) A physical analysis of the severe 2013/2014 cold winter in North America. J Geophys Res Atmos 120:149–165. doi:10.1002/2015JD023116

Yu B, Zwiers F (2007) The impact of combined ENSO and PDO on the PNA climate: a 1000-year climate modeling study. Clim Dyn 29:837–851

Yu B, Lin H, Wu Z, Merryfield W (2016) Relationship between North American winter temperature and large-scale atmospheric circulation anomalies and its decadal variation. Environ Res Lett 11:074001. doi:10.1088/1748-9326/11/7/074001

Zhang T, Hoerling MP, Perlwitz J, Sun DZ, Donald M (2011) Physics of US surface temperature response to ENSO. J Clim 24:4874–4887